Acta Materialia 265 (2024) 119634

Contents lists available at ScienceDirect

Acta Materialia

journal homepage: www.elsevier.com/locate/actamat

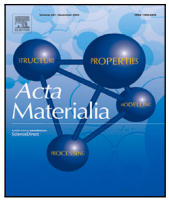

Full length article

# Enhanced diffusion in thin-film Cu-Zr nanoglasses

C. Aaron Rigoni [a,*], Evgeniy Boltynjuk [b], Hendrik Voigt [a], Harald Rösner [a], Bonnie Tyler [c], Horst Hahn [b,d], Sergiy V. Divinski [a], Gerhard Wilde [a]

[a] Institute of Materials Physics, University of Münster, Wilhelm-Klemm-Str. 10, Münster, 48149, Germany
[b] Institute of Nanotechnology, Karlsruhe Institute of Technology, Hermann-von-Helmholtz-Platz 1, Eggenstein-Leopoldshafen, 76344, Germany
[c] University of Münster, Physikalisches Institut and Center for Soft Nanoscience, Wilhelm-Klemm-Str. 10, Münster, 48149, Germany
[d] University of Oklahoma, School of Sustainable Chemical, Biological and Materials Engineering, 201 Stephenson Pkwy., Norman, OK, 73019, United States

ARTICLE INFO

*Keywords:*
Nanoglass
Diffusion
Ion beam sputtering
ToF-SIMS
Magnetron sputtering
Excess free volume
Relaxation

ABSTRACT

Tracer measurements with both radioactive, $^{55}$Fe, as well as natural, mainly $^{56}$Fe, isotopes are used to investigate Fe diffusion in a Cu-Zr nanoglass in comparison to their diffusion rates in a homogeneous amorphous counterpart. The columnar-structured nanoglass and the homogeneous amorphous films are synthesized using radio-frequency magnetron sputtering. Ion beam sputtering (with the $^{55}$Fe radioisotope) and time-of-flight secondary ion mass spectroscopy (with natural Fe) are used for the diffusion experiments. Remarkably, faster Fe diffusion is observed in the columnar nanoglasses, supporting the concept of glass–glass interfaces. The relative diffusion enhancement is explained within the excess free volume concept that is supported by structural investigations using transmission electron microscopy. For the first time, the relaxation dynamics in a nanoglass as well as in a homogeneous thin-film glass of identical composition are evaluated via time-dependent diffusion measurements.

## 1. Introduction

One of the most impactful strategies for equi-compositionally enhancing the properties of a material with a crystalline structure involves tuning the concentration of defects within it. It is widely recognized that increasing the defect concentration can yield significant improvements in e.g. mechanical properties [1,2] as well as enhancements of diffusivity [3]. Until recently, these effects could not be harnessed in amorphous materials, such as metallic glasses, due to the absence of localized and tunable structural defects. However, the concept of nanoglasses has emerged as a promising avenue, aiming to combine the advantages of glassy materials with the potential to fine-tune their properties through the introduction of structural defects [4].

In this sense, nanoglasses are composed of nanometer-scale amorphous domains (i.e. "cores"), separated by amorphous interfaces that present the structural "defects". Previous investigations have unveiled that these materials can exhibit superior properties compared to their homogeneous amorphous counterparts. Notable examples include reduced density, a lower coordination number of nearest-neighbor atoms, distinct electronic structures [5], or an elevation of the ferromagnetic transition temperature [6].

Today, several established methods facilitate the synthesis of nanoglasses. For instance, inert gas condensation (IGC) [7–9] and magnetron sputtering [10–12] are two prevalent techniques, where magnetron sputtering of columnar films offers a versatile and reproducible approach. By carefully adjusting the settings the deposition process can be optimized to create columnar structured films with a nanoglass structure [12]. While the synthesis of columnar structured amorphous films has been previously documented [13,14], the fabrication of a nanoglass using this particular method is considered to be a novel advancement.

This present study is centered around tracer diffusion measurements of $Cu_{60}Zr_{40}$ nanoglasses produced via magnetron sputtering. The combination of copper and zirconium as principal constituents for a metallic nanoglass has been explored in previous studies, yielding insights into (micro)structure evolution [15] or notch sensitivity [16] via molecular dynamics simulations. Moreover, there exists experimental evidence of enhanced thermal stability, increased mechanical properties [17], or the existence of glass–glass interfaces and their structural distinction to the glassy cores [18].

Diffusion measurements have consistently served as a sensitive tool to probe structural alterations [19–21], particularly in disordered materials where imaging techniques face limitations. Radiotracer diffusion, in particular, proves versatile across a wide spectrum of diffusion depths and corresponding diffusion coefficients due to its exceptional

* Corresponding author.
*E-mail address:* aaron.rigoni@uni-muenster.de (C. Aaron Rigoni).

https://doi.org/10.1016/j.actamat.2023.119634
Received 6 September 2023; Received in revised form 1 December 2023; Accepted 26 December 2023
Available online 28 December 2023

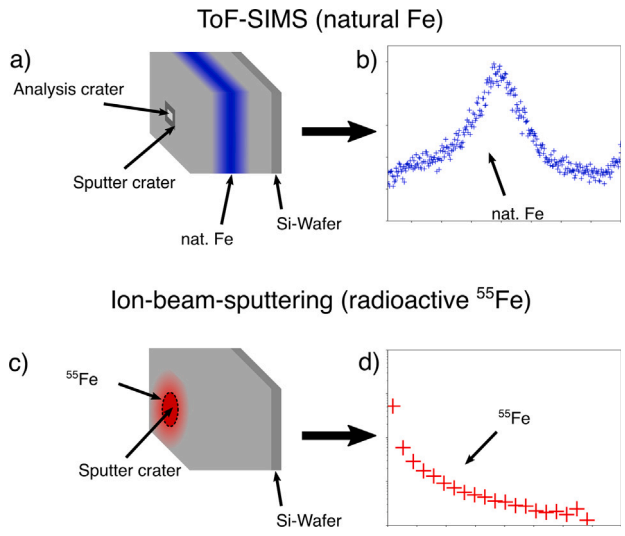


**Fig. 1.** (a) "Sandwich"-like sample design used for ToF-SIMS analysis. $Cu_{60}Zr_{40}$ is sputtered on a Si-wafer and at half-thickness of the sample a thin layer of natural Fe is co-sputtered. ToF-SIMS analysis is done using a dual beam setup with one beam for sputtering and one for analysis. (b) Schematic depth profile obtained by ToF-SIMS showing a typical Gaussian-type peak for Fe. (c) $Cu_{60}Zr_{40}$ sputtered on a Si-wafer with a $^{55}$Fe isotope deposited on the surface. An aperture (of ~3.5 mm) attached to the center of the sample surface induces a disk-shaped crater during subsequent ion beam sputtering with $Ar^+$ ions. (d) Schematic concentration–depth profile obtained by ion beam sputtering for the $^{55}$Fe tracer.

detection efficiency. While mechanical grinding is generally suited for relatively deep diffusion lengths beyond a few microns, ion beam sputtering offers a convenient means to examine even extremely shallow tracer penetration profiles down to diffusion depths below 100 nm [22].

Extensive research has been devoted to the diffusion behavior in conventional glasses, including metallic glasses, unraveling intricate insights into glassy dynamics [23–26]. While the diffusion coefficient is often deemed time-independent in crystalline materials, it has been demonstrated that this assumption does not hold for most glassy materials at temperatures well below the glass transition [23,24,27–29]. This behavior originates from the specific relaxation processes in glasses that reflect the underlying so-called "glassy dynamics", featuring a wide spectrum of relaxation processes and relaxation times. In glasses relaxed (or "aged") for a long time, the diffusion coefficients follows an Arrhenius relationship. Thus, diffusion measurements on aged glasses can reveal the activation enthalpy, $Q$, that is correlated with the size of the solute atoms [25] and the composition [30]. The pre-exponential factor for diffusion, $D_0$, is thought to provide valuable information about the excess volume stored within the glassy material [31].

Considering the presence of characteristic interface-like structures within nanoglasses [1], it is reasonable to anticipate an increase in excess volume, thereby favoring enhanced diffusion rates in nanoglasses as well as an impact of the glass–glass interfaces on the relaxation behavior and thus on the time dependence of diffusion. The current work presents the results of the first in-depth tracer diffusion analysis on a nanoglass.

## 2. Methods

### 2.1. Sample preparation

Thin film samples were prepared from an alloy target of nominal composition of $Cu_{60}Zr_{40}$ (at.%) using radio-frequency (RF) magnetron sputtering to fabricate samples for two different experimental measurement techniques: time-of-flight secondary ion mass spectroscopy (ToF-SIMS), Fig. 1(a) and (b), and ion beam sputtering (IBS), Fig. 1(c) and (d).

The magnetron sputtering system was used with a fixed distance between the substrate, target of 100 mm and a target tilt angle of 20°. A background pressure in the deposition chamber below $5.0 \times 10^{-8}$ mbar was reached before deposition. Thin films were deposited continuously on Si (100) wafers with a native oxide layer cut in pieces with a size of $7 \times 7$ mm. Sputtering was performed at a substrate temperature of 293 K and a power of 100 W with a substrate rotation velocity of 10 rpm.

As it was stated, films of two types, with either a homogeneous structure or a columnar nanoglass one, were prepared. The homogeneous films were deposited at a working pressure of $2.8 \times 10^{-3}$ mbar and a constant Ar flow rate of 40 Sccm. Columnar films were deposited at a working pressure of $8 \times 10^{-3}$ mbar and a constant Ar flow rate of 100 Sccm. Sputtering times were adjusted to reach a thickness of about 1 μm for IBS and about 400 nm for ToF-SIMS measurements. The thicknesses of the films were measured with a *Veeco Dektak 6M Stylus Profiler* and by scanning electron microscopy (*SEM LEO 1530, Carl Zeiss AG*).

For the ToF-SIMS measurements, a thin tracer layer of natural Fe was co-sputter-deposited at middle thickness of the thin film sample, using a second magnetron gun equipped with an iron target. Thus, the sputter deposition of CuZr was not interrupted during the synthesis process.

### 2.2. ToF-SIMS

Fe-containing homogeneous and columnar nanoglass samples were annealed in a vacuum furnace under vacuum below $5 \times 10^{-8}$ mbar, at temperature of 573 K for 4 days, 598 K for 2 days, 623 K for 1 days, 648 K for 3 h and 673 K for 1 h. At each temperature, the samples of homogeneous and columnar nanoglass were annealed in the furnace at the same time. The temperature during annealings was controlled by a Chromel-Alumel thermocouple with an accuracy of 2 K.

Diffusion measurements using ToF-SIMS were performed using a custom-built instrument, which is equivalent to the IONTOF M6 commercial version. The ToF-SIMS was operated at a pressure of $<10^{-8}$ mbar. Depth profiles, mainly of the $^{56}$Fe isotope (about 92% natural abundance), were measured in a dual-beam mode, using a 30 keV $Bi^{3+}$ primary ion source with a pulsed current of 0.02 pA for analysis and a 2 keV $O^{2+}$ source with a current of 500 nA for sputtering. Analysis was conducted over $100 \times 100$ μm$^2$ areas and sputtering was conducted over $500 \times 500$ μm$^2$ areas. Depth calibration was achieved assuming a constant sputtering rate and ensuring that the iron peak was positioned at the midpoint of the depth profile.

### 2.3. Ion beam sputtering

$^{55}$Fe dissolved in HCl and highly diluted in double distilled water was used as a tracer element for the radio tracer diffusion analyses. About 1 to 3 μl of the solution, equivalent to 5 to 10 kBq activity, is placed on the center of the sample surface and dried, Fig. 1(c). The sample is placed in a vacuum furnace system, where the chamber is pumped to a pressure better than $10^{-6}$ mbar and afterwards purged with purified Ar gas (5N) and subsequently remains in this atmosphere for the respective diffusion time and the selected diffusion temperature (at temperature of 573 K for 7 days; 598 K for 5 days; 623 K for 1 days; 648 K for 3 h and 673 K for 1 h). After annealing, the sample is cleaned using cotton sticks with ethanol to remove remaining radiotracer from the surface. It is then placed in the sputtering chamber which is pumped to a vacuum of about $10^{-6}$ mbar. An $Ar^+$ plasma emitted by a *3 cm DC Ion Source* ion gun, with an acceleration voltage of 1 kV and a beam current of 20 mA, impacts the center of the sample's surface that is isolated by an aperture. The material that is sputtered-off is caught on a foil which is spooled on a cassette and subsequently separated into 20 to 40 individual sections. The sections are individually dissolved

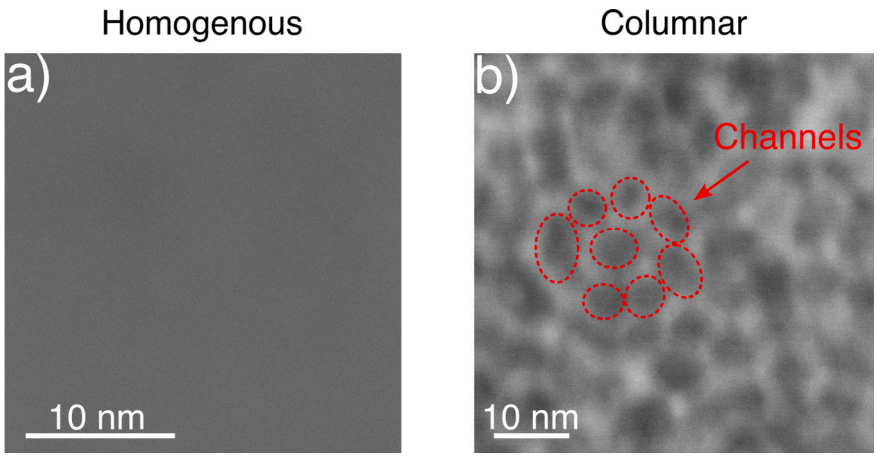


**Fig. 2.** HAADF-STEM image showing top views of (a) the homogeneous thin film glass and (b) the columnar structure of the CuZr nanoglass.

and analyzed in a liquid scintillation counter (LSC, *TRI-CARB 2910TR, Perkin Elmer*).

To calculate the depth of the sputtered area, the mass difference before and after the sputtering is measured using a microbalance (*Satorius Supermicro S4*) with an accuracy of $10^{-4}$ mg. A constant sputtering rate has been assumed. The sputter current has been controlled and was found to be constant within ±5%.

## 3. Results and discussion

### 3.1. Characterization

Structural analysis was conducted using an *FEI Titan Themis 60–300 (Thermo Fisher Scientific)* transmission electron microscope (TEM) equipped with an image $C_s$ corrector and a monochromator.

The samples were analyzed by high-angle annular dark field scanning transmission electron microscopy (HAADF-STEM). Fig. 2 indicates HAADF-STEM images in top view for both structure types. While the nanoglass sample features a grain-like structure with darker channels and a brighter matrix, a uniform contrast distribution, as expected, is obtained for the homogeneous amorphous film. The amorphicity, i.e. the absence of crystalline fractions of the structures was confirmed for both samples [18]. Previous TEM studies also revealed that during the sample production a significant amount of up to 35 at.% oxygen was introduced into the sample and further investigations using X-ray photoelectron spectroscopy (XPS) showed that this leads to a mixture of metallic and oxide bonding states. For a more detailed description of the TEM sample preparation, microstructural and chemical analysis, the interested reader is referred to [18].

### 3.2. ToF-SIMS measurements

For ToF-SIMS analyses, the samples were sputtered until the signal of the Si-substrate was measured. As an example, a raw ToF-SIMS profile is shown in Fig. 3 for the initial (as-prepared) columnar nanoglass sample. All measured intensities were divided by the values corresponding to the Cu signal which is the major component of the alloy. This procedure eliminates all device influences and potential variations of the sputtering rates. The peak signal corresponding to the deposited natural Fe was fitted by a Gaussian function and defined as the middle point of the sample. Together with the measured thickness of the film a proper depth calibration was obtained for the entire measurement, where the peak position of the Fe tracer was defined as the zero position of the depth coordinate $x$.

Diffusion-induced broadening was observed in both (positive and negative $x$) directions with respect to the defined zero position, but for the further evaluation only the flank of the tracer peak pointing to the original free surface of the film, i.e. the left-hand side from the peak in Fig. 3, was used for the analysis to minimize the artefacts from sputter broadening.

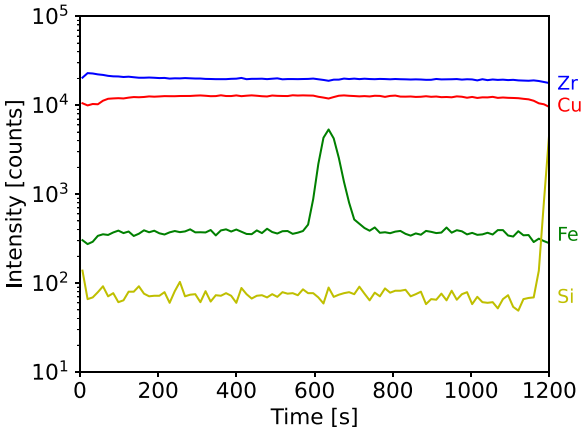


**Fig. 3.** ToF-SIMS profiles of the columnar sample in the as-deposited state. While the Fe signal shows a peak in the center of the sample, the Zr and Cu signals remain virtually constant. The Si signal corresponds to the background and rises at the end of the measurement when the Si substrate was reached.

Using the thin film solution of the diffusion equation for infinitely thick samples [32], the depth profiles obtained on the as-deposited films were fitted by Gaussian functions:

$$C(x) = \frac{M_0}{\sqrt{\pi D t}} \cdot \exp\left(-\frac{x^2}{4Dt}\right) + C_{bcgr}, \tag{1}$$

where $M_0$ is the initial tracer amount, $x$ the depth, $t$ the annealing time, $D$ the diffusion coefficient, and $C_{bcgr}$ the background intensity.

For the annealed columnar samples, the semi-infinite-sample approximation in Eq. (1) is not fulfilled anymore, since Fe diffusion was sufficiently fast to penetrate the entire thickness of the nanoglass film. Thus, a finite-system solution was used as the fitting function of the diffusion profile [33]:

$$C(x) = \frac{1}{2}C_0 \cdot \sum_{n=-\infty}^{\infty}\left\{\mathrm{erf}\left(\frac{h+2nl-x}{2\sqrt{Dt}}\right) + \mathrm{erf}\left(\frac{h-2nl+x}{2\sqrt{Dt}}\right)\right\}, \tag{2}$$

where $l$ is the thickness of the sample and $h$ is a factor considering the thickness of the deposited layer (used as a fitting parameter).

In Fig. 4(a) the diffusion broadening is shown for the columnar (nanoglass) sample. The plot shows the intensity of the Fe/Cu signal ratio for the initial, as-deposited sample in comparison to the Fe/Cu signal ratio after annealing for one hour at 673 K, which is

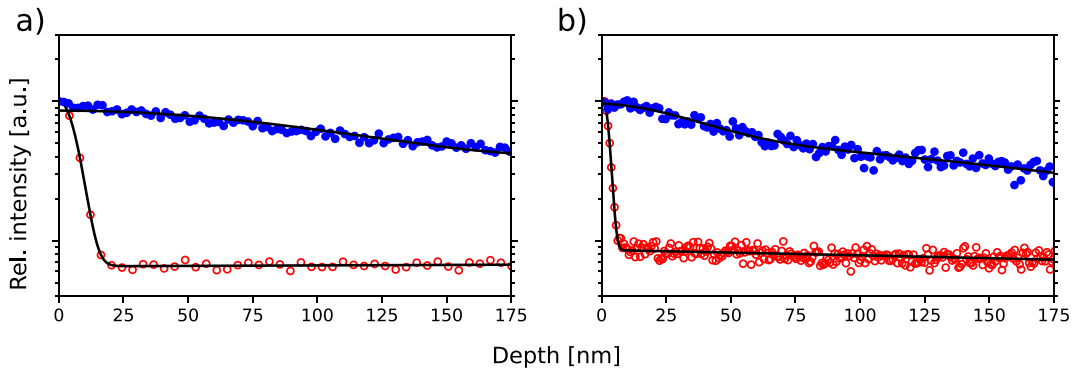


**Fig. 4.** Diffusion profiles measured for nano- (a) and homogeneous (b) glasses at 673 K as analyzed by ToF-SIMS. As-deposited initial (red open symbols) and diffusion-annealed (blue closed symbols) profiles are compared. The intensity of the Fe/Cu ratio is normalized to the starting value. (For interpretation of the references to color in this figure legend, the reader is referred to the web version of this article.)

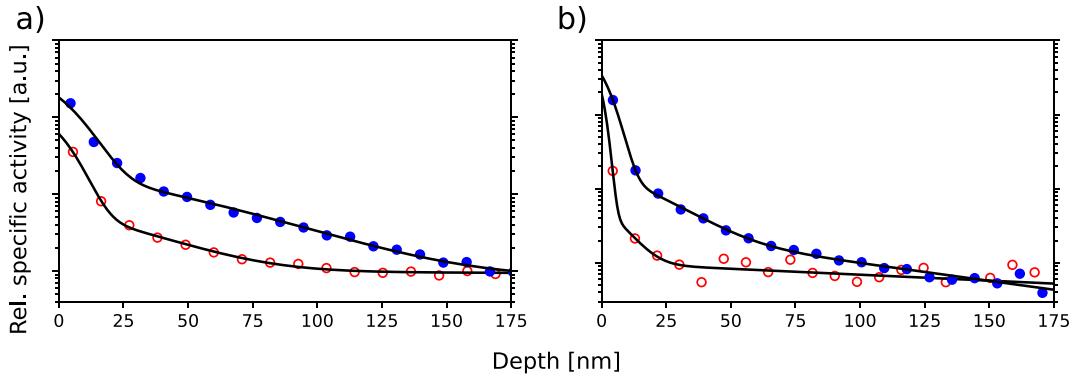


**Fig. 5.** Diffusion profiles measured for nano- (a) and homogeneous (b) glasses at 673 K using ion beam sputtering (blue closed symbols). The diffusion profiles obtained after spike-annealing treatments, see text, are shown by red open symbols. The solid lines correspond to the fits according to Eq. (3). (For interpretation of the references to color in this figure legend, the reader is referred to the web version of this article.)

the highest temperature used in this work. The respective diffusion profiles obtained at identical temperatures and diffusion times for the homogeneous amorphous thin film sample are shown in Fig. 4(b).

The tracer diffusion coefficients are calculated by subtracting the diffusion-related broadening of the initial profile from the profiles obtained on the annealed samples.

### 3.3. Ion beam sputtering measurements

The activities measured by the liquid scintillation counter followed by background subtraction are then divided by the section mass and thus transformed into the specific activities. Since the activities are not calibrated to the absolute rates of the radioactive decays, we have plotted and analyzed the relative specific activities, which is sufficient for a reliable estimation of the diffusion rates in the present case. The data are fitted distinguishing three contributions:

$$C(x) = \underbrace{C_1 \cdot \mathrm{erfc}\left(\frac{x}{\sigma_1}\right)}_{\text{Surface effects}} + \underbrace{C_2 \cdot \mathrm{erfc}\left(\frac{x}{\sigma_2}\right)}_{\text{Diffusion broadening}} + \underbrace{C_3 \cdot \exp(-\sigma_3 x)}_{\text{Sputter broadening}}, \tag{3}$$

where $C(x)$ is the relative specific activity, $x$ the penetration depth, and $C_1$, $C_2$, $C_3$, $\sigma_1$, $\sigma_2$ and $\sigma_3$ are the respective fitting parameters, and erfc denotes the complementary error function.

The diffusion coefficients, $D$, are calculated using the parameter $\sigma_2$, whereas $\sigma_1$ leads back to surfaces effects for the initial tracer solution. The exponential function corresponds to a fraction of the tracer broadening caused by the sputtering [34] alongside with some contribution to the second term in Eq. (3).

Moreover, a so called spike annealing was used to evaluate precisely the zero profile and thus the sputtering-induced transformation of the real concentration profile. For this reason, a sample deposited with tracer was annealed for less than 5 min to bond the radiotracer material to the sample surface. This profile corresponds to a "zero" diffusion depth and allows a careful evaluation of the profile broadening induced by ion beam sputtering [22].

In Fig. 5(a), the profiles obtained after spike-annealing and after annealing at 673 K are shown for the columnar-structured nanoglass sample; a broadening of the profile obtained after annealing at 673 K is clearly observed. Furthermore, the sputtering-induced effects are clearly seen as deviations from an anticipated $\delta$-function like profile.

In the same way the results obtained for the homogeneous amorphous thin-film sample after spike-annealing and after annealing at 673 K are presented in Fig. 5(b). A clear difference between the profiles corresponding to the spike- or diffusion annealing at 673 K is visible. Furthermore, it is noticeable that sputtering-induced effects are material-depended, when comparing the profiles measured after the spike annealing treatments on columnar and homogeneous samples shown in Fig. 5.

The respective diffusion coefficient $D$ at a temperature $T$ is then determined by subtracting the profile broadening induced by the spike annealing,

$$D = \frac{\sigma_2^2 - \sigma_{2,\mathrm{Spike}}^2}{4t}. \tag{4}$$

An important note is due here. The presence of fast diffusion pathways, which correspond to the regions with a higher excess free volume, raises an important question regarding an appropriate scheme for analyzing diffusion profiles. In the case of nanoglasses, the existence of glass/glass interfaces can formally be considered equivalent to the presence of grain boundaries in crystalline materials. Therefore, a similar analysis of concentration profiles may be required.

The analysis of grain boundary diffusion is formally based on the Fisher model [35], and the specific analytical approach depends on the kinetic regime introduced by Harrison [36] for a homogeneous polycrystalline material [37]. Let us consider our nanoglass, which consists of columns with a size of ten nanometers separated by a few nanometer thick matrix region, as shown in Fig. 2. Due to the increased excess free volume in the columnar structures, we can assume that the corresponding diffusion coefficients $D_{col}$, are larger than those for the separating matrix, $D_m$. In other words, $D_{col} > D_m$ or even $D_{col} \gg D_m$. This leads to an "inverted" grain boundary diffusion model, where the presence of "grain boundaries" in the matrix material retards diffusion compared to the columnar material. Note that this situation is formally similar to that observed previously for Au diffusion in polycrystalline Si [38,39] and for the analysis of the corresponding GB diffusion problem one may use the formalism developed in those papers.

Under the present conditions, which correspond to the A-type kinetics according to Harrison's classification, where $\sqrt{D_{col}t} > d$ (with $d$ being the diameter of the columns), we expect a single contribution to the resulting penetration profile. This means that there will not be a separate "grain boundary tail", and an *effective* diffusion coefficient, $D^{eff}$, can be measured. $D^{eff}$ is calculated as $D^{eff} = (1 - f)D_{col} + fD_m$, without considering potential solute segregation at the "grain boundaries". Here $f \approx 3\delta/d$ represents the volume fraction of the grain boundary material, with $\delta$ being the width of the "grain boundary".

This formalism can be applied to the case of diffusion in a nanoglass in a relatively straightforward manner. However, in our specific case, the measured effective diffusion coefficients will represent weighted sums of the diffusion coefficients mentioned above, without knowing the exact relationships between them. Additionally, since we are measuring the diffusion of Fe, it is expected that there will be some segregation of Fe atoms to the glass/glass interfaces. This segregation needs to be properly taken into account if we want to estimate the values of $D_{col}$ and $D_m$ separately. Since any such estimate would involve a number of approximations and speculations, we are reporting the effective values $D$ here, Eq. (4).

### 3.4. Relaxation

The diffusion rates in glasses depend strongly on their relaxation state and may be time-dependent [40,41]. Since a time-independent diffusivity, $D^*$, can only be measured in a completely relaxed sample, one has generally take the evolution of the diffusion coefficients during the annealing time, $t$ into account:

$$D = 1/t \int_0^t D'(t')dt' \tag{5}$$

where $D'(t')$ is the diffusion coefficient at the time $t'$. To evaluate this behavior, time-dependent radiotracer diffusion measurements were performed at a constant temperature. A temperature of 573 K was chosen, because the relaxation times for the higher temperatures are likely too fast to observe a significant time dependence of the diffusivity.

While the usual annealing time was 7 days at this temperature, diffusion annealing treatments were performed for both, shorter and longer times. For the homogeneous samples, shown in Fig. 6 (blue bars), annealing treatments for 24 h, 14 days and 7 days were used. Moreover, the diffusion coefficient measured for a relaxed sample is indicated by a horizontal line. In this work, a "relaxed" sample is defined as a sample annealed for 14 days at 573 K before applying the tracer on the sample surface. Since diffusion in the nanoglass (Fig. 6, red bars) is significantly faster, reliable measurements of the penetration profiles created by annealing for 14 days was not possible, because the tracer would diffuse through the entire thickness of the sample and formally $\sigma_2 \to \infty$ in Eq. (3).

Fig. 6 suggests the existence of certain relaxation processes in both nanoglassy — and homogeneous samples. Indeed, the measured effective diffusion coefficients decrease towards the values established

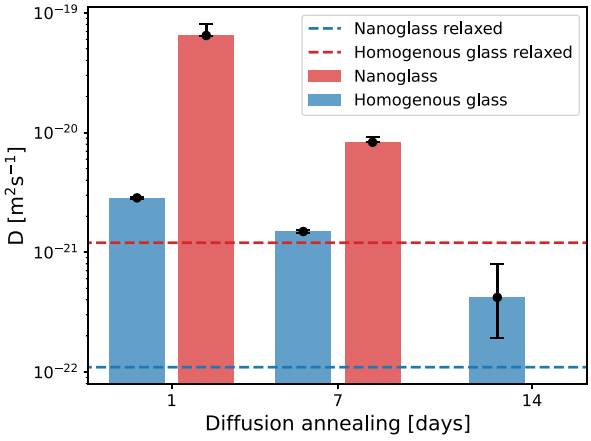


**Fig. 6.** The measured diffusion coefficients at 573 K as function of the diffusion time. For the homogeneous glass (blue bars) the samples were annealed for 1, 7, and 14 days. The columnar nanoglass (red bars) was annealed for 1 and 7 days. For both sample systems another measurement was performed on a relaxed state (prepared by annealing at 573 K for 14 days before applying the tracer), setting the diffusion annealing to 7 days. The corresponding diffusion coefficients are indicated by horizontal lines. (For interpretation of the references to color in this figure legend, the reader is referred to the web version of this article.)

for the relaxed state with increasing diffusion time. This has to be considered in the interpretation of the diffusion data. Considering the inherent variability in the relaxation process, where different annealing temperatures would require varying annealing times, it is impractical to achieve complete relaxation for the "sandwich" samples. Therefore, to ensure comparability, similar temperature and annealing time parameters are selected for both the homogeneous and the nanoglass samples. This approach allows for the attainment of comparable results, which is the primary objective of the current study.

### 3.5. Temperature dependence of the diffusivities

The determined tracer diffusion coefficients are shown in an Arrhenius plot for the columnar nanoglass (Fig. 7(a)) and the homogeneous glass (Fig. 7(b)). Based on a direct comparison of the measured values, it is evident that the diffusion rates of Fe are higher in the nanoglass samples, as depicted in Fig. 8. In general, the diffusion coefficients obtained from two distinct methods exhibit similar magnitudes, indicating an acceptable level of agreement.

By fitting a common Arrhenius-type function to the diffusivities measured by IBS and ToF-SIMS, the activation enthalpy, $Q$, of Fe diffusion in the two glassy states is determined. The activation enthalpy is found to be $(1.43 \pm 0.22)$ eV for the columnar sample, while it is $(1.65 \pm 0.14)$ eV for the homogeneous sample. The results indicate that the values of $Q$ are similar within the uncertainties for the two glassy states. The obtained values for $Q$ are generally in the range that can be expected for tracer diffusion in a metallic glass, see e.g. a review of Faupel et al. [41].

A thorough examination of Fig. 7 reveals that the deviations between the diffusion coefficients measured by the Time-of-Flight Secondary Ion Mass Spectrometry (ToF-SIMS) or Ion Beam Sputtering (IBS) techniques at the same temperature are somewhat larger for the columnar nanoglass samples compared to the measurements conducted on the homogeneous amorphous samples. This observation suggests the presence of heterogeneity in the thin films on a millimeter or submillimeter scale. The area analyzed by IBS, determined by the aperture diameter of approximately 3.5 mm, is significantly larger than the sputtered area of $100 \times 100\,\mu m^2$ acquired by ToF-SIMS. In the case of the homogeneous amorphous samples, the small deviations between the two techniques confirm a fully homogeneous structure. However,

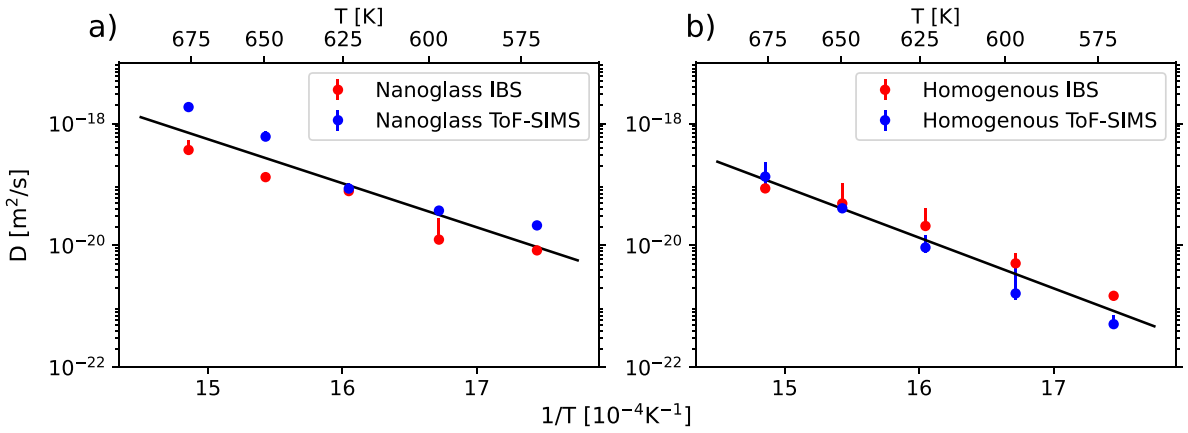


**Fig. 7.** Arrhenius diagrams for the diffusion coefficients measured for the columnar CuZr nanoglass (a) and the homogeneous glass (b) determined by either ion-beam sputtering (red symbols) or ToF-SIMS analysis (blue symbols). (For interpretation of the references to color in this figure legend, the reader is referred to the web version of this article.)

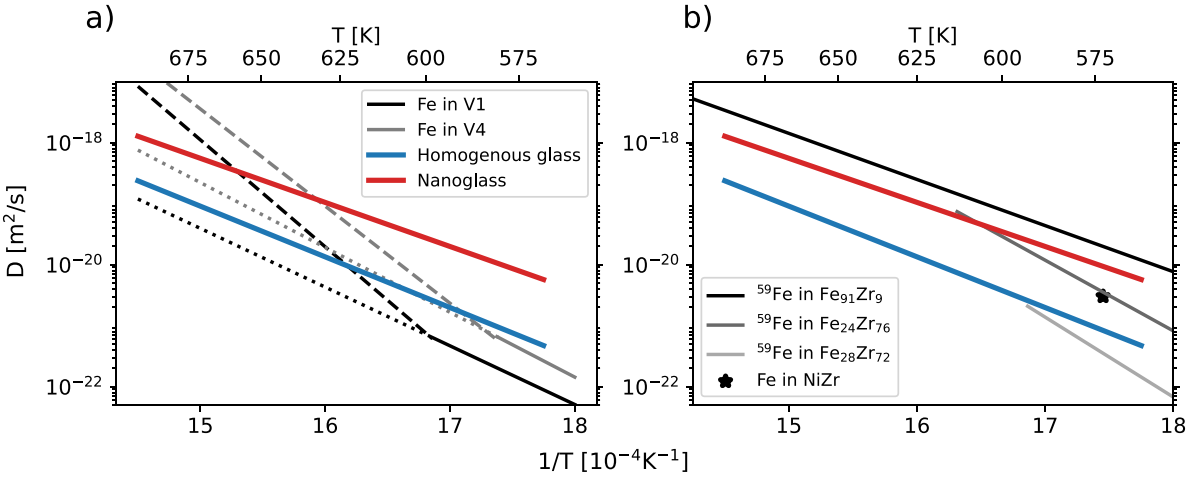


**Fig. 8.** (a) Fe diffusion rates for the homogeneous glass (blue lines) and the nanoglass (red lines) determined in the present study in comparison to the diffusion rates of Fe in Vitreloy 1 (black line) and Vitreloy 4 (gray line) [30]. The values determined in this work for the homogeneous glass are generally in line with the data for the Vitreloys below the kink (solid lines). At higher temperatures, the Vitreloys show a kink behavior which is indicated by dashed lines. As a guide to the eye, the low-temperature diffusivities are extrapolated as dotted lines. (b) Comparison of the diffusion rates for the homogeneous glass and the nanoglass with the diffusion rates measured for $^{59}$Fe in amorphous FeZr with varying composition [42]. The diffusion coefficient of Fe in amorphous NiZr measured at 573 K [43] is marked by a black star. (For interpretation of the references to color in this figure legend, the reader is referred to the web version of this article.)

for the nanoglass samples, local heterogeneity in the structure is expected [18]. This heterogeneity on the micrometer scale may arise from regions with significantly higher or lower frequencies of channels within the sample. It is important to note that the SIMS analysis and the radiotracer method have previously demonstrated good reproducibility for crystalline materials [44].

### 3.6. Estimation of the excess free volume

Given the absence of significant changes in the activation enthalpy, it is reasonable to suggest that the higher diffusivities of the columnar nanoglass are related to differences of the diffusion pre-factors $D_0$.

Indeed, using a model based on the assumption of excess volume-related "diffusion defects" [45], the pre-factor $D_0$ can be written as [31],

$$D_0 = \gamma a^2 f \nu c_d \exp(S/k), \tag{6}$$

where $\gamma$ is a geometrical factor, $a$ the jump distance, $f$ the correlation factor, $\nu$ the jump attempt frequency, $c_d$ the concentration of "diffusion" defects, $S$ the activation entropy and $k$ the Boltzmann constant. The main parameter of the model, the "diffusion defect" concentration, $c_d$, is given by $\exp(-\gamma\Omega^*/\Omega)$, where $\Omega^*$ is the critical volume needed to create a "diffusion defect" and $\Omega$ is the excess free volume in a glass [31].

By assuming that $\gamma$, $a$, $f$, $\nu$ and $S$ are approximately the same for the homogeneous amorphous glass and the nanoglass, the ratio between the diffusion pre-factors is given by:

$$\frac{D_0^{\text{hom}}}{D_0^{\text{col}}} = \exp\left(-\gamma\Omega^*\left[\frac{1}{\Omega_{\text{hom}}} - \frac{1}{\Omega_{\text{col}}}\right]\right) \tag{7}$$

Furthermore, introducing $\Delta$ as the relative increase of the excess free volume in the nanoglass, $\Omega_{\text{col}}$, with respect to that in the homogeneous glass, $\Omega_{\text{hom}}$, we may write $\Omega_{\text{col}} = \Omega_{\text{hom}}(1+\Delta)$. Since $c_d$ in the relaxed glassy alloys is estimated [31] as $\sim 10^{-6}$, we arrive at $\gamma\Omega^*/\Omega_{\text{hom}} = -\ln(c_d) = \ln(10^6)$.

Since the fitted value for $D_0$ usually has large uncertainties exceeding an order of magnitude, the above estimate was applied to the ratios of the absolute diffusion rates, $D^{\text{hom}}/D^{\text{col}}$. In this way we obtain ten values for $\Delta$, one for every temperature and measurement method. From these values the average and standard deviation are calculated. As a result, the value of $\Delta$ is estimated as $(18 \pm 10)\%$.

It has to be stated at this point that the difference estimated from the diffusion data is averaged over a large sample area containing a huge number of channels, so that a change of about 18% on average seems quite reasonable, accounting also for the approximations made.

A previous study [18] using nano-beam diffraction patterns to determine changes of the specific volume via analyzing the shift of the magnitude of the $k$-vector of the dominant diffraction ring arrived at a value for the difference of the specific volume of matrix and channels between 10% to 28% for a columnar structured $Cu_{60}Zr_{40}$ nanoglass. Those changes also include density changes caused by variations of the composition. Considering the changes of the compositions of matrix and interface regions (i.e. "channels") leads to a difference of the excess volume of $(10 \pm 6)\%$. It should be noted that typical changes of the excess volume caused by relaxation or rejuvenation are less then 2% [46–50]. The changes of the excess volume observed by TEM and diffusion exceed this value by far and indicate significant differences of the atomic structure between homogeneous and nanoglasses.

The present comparison corresponds to a view that the "matrix" in the nanoglass reveals a similar structure as that of the homogeneous glass, while the "channels" represent the regions with an enhanced excess free volume.

### 3.7. Diffusion in zr-based glasses

In Fig. 8(a) the diffusion rates measured in this work are compared with the diffusion data reported for Fe in Vitreloy 1 (V1, $Zr_{41}Ti_{14}Cu_{12.5}Ni_{10}Be_{22.5}$) and Vitreloy 4 (V4, $Zr_{46.75}$ $Ti_{8.25}$ $Cu_{7.5}$ $Ni_{10}$ $Be_{27.5}$) glasses [30]. The data suggests that the absolute values of the diffusion coefficients are relatively similar, although characteristic deviations of the temperature dependencies are apparent. The activation enthalpy is significantly higher for the Vitreloy materials compared to the homogeneous- and nanoglass thin films in the high temperature region, above about 600 K (Fig. 8(a); dashed lines). On the other hand, the effective activation enthalpies of diffusion below 600 K (Fig. 8(a); solid lines) in both Vitreloy glasses become significantly lower, with $Q$ found to be $(1.91 \pm 0.2)$ eV and $(2.11 \pm 0.2)$ eV respectively, and they match closely those determined for the homogeneous- and the nanoglass thin films.

This comparison provides a further strong hint that the deposited thin film samples investigated in this work are in a non-relaxed state. Moreover it shows the difference between the diffusion behavior of sputtered samples in comparison with bulk glasses. After sputtering, the samples seem to be in a less relaxed state compared to the rapidly quenched Vitreloy samples. This difference can be explained by the different effective cooling rates of the different preparation methods.

Additionally, it is worth comparing these values to those of the binary amorphous $Ni_{50}Zr_{50}$ alloy. Previous research [43] reported Fe diffusion in this alloy at a single temperature of 573 K, with a diffusion coefficient of $3 \times 10^{-21}$ $m^2$ $s^{-1}$, which closely aligns with the values obtained for the homogeneous amorphous sample in our current study (Fig. 8(b)). Furthermore, the estimated activation enthalpy ($Q$ = 1.64 eV) for $Ni_{50}Zr_{50}$ [43] is similar to the values documented here.

Moreover, Fe diffusion rates were measured in other binary alloys containing Zr by Hovath et al. [42] using FeZr, as shown in Fig. 8(b). Generally, the diffusion rates increase with higher Fe content, while still remaining close in magnitude to those ones obtained for the homogeneous glass and the nanoglass. Notably, for the $Fe_{28}Zr_{72}$ and $Fe_{24}Zr_{76}$, the activation enthalpy is significantly higher at 2.3 eV and 2.6 eV, respectively. On the other hand, for $Fe_{91}Zr_9$, the activation enthalpy is of the order of 1.5 eV, similar to the values obtained in this study.

## 4. Summary and conclusions

Thin film $Cu_{60}Zr_{40}$ nanoglasses and homogeneous amorphous glasses were produced using magnetron sputtering. Tracer diffusion measurements were performed using ion beam sputtering as well as ToF-SIMS analyses. Enhanced diffusivities related to the glass–glass interfaces in the nanoglasses are observed. In fact, significantly higher diffusivities are measured for the nanoglass in the entire range between 573 K and 673 K when compared to the homogeneous amorphous counterpart.

Moreover, a quantitative estimate of the excess volume difference between the nanoglass and the homogeneous glass of similar chemical composition was obtained. The result shows an increase in excess volume of about 18% for the nanoglass state. This value is significantly larger as any relaxation-induced density changes and also fits well with previous measurements using TEM-based local methods.

Additionally, the annealing time for the diffusion measurements was varied to obtain insights about the relaxation kinetics in a nanoglass for the first time. The results indicate that both sample types, homogeneous glass and nanoglass are not in a fully relaxed state, especially at the lower temperatures investigated here. Thus the diffusivity decreases with increasing annealing time. With the strongly increased excess volume of the nanoglass, this behavior is somewhat unexpected and indicates that local structures and bonding types need a thorough investigation.

## Declaration of competing interest

The authors declare that they have no known competing financial interests or personal relationships that could have appeared to influence the work reported in this paper.

## Data availability

The data that support the findings of this study are available from the corresponding author upon reasonable request.

## Acknowledgments

Financial support from the German Science Foundation (DFG - project number WI-1899/42-1 and HA-1344/46-1) is acknowledged. The DFG is further acknowledged for funding our TEM equipment via the Major Research Instrumentation Program under INST 211/719-1 FUGG. The authors would like to thank the Karlsruhe Nano Micro Facility (KNMFi) at Karlsruhe Institute of Technology (KIT) for the use of facilities.

## Appendix A. Supplementary data

Supplementary material related to this article can be found online at https://doi.org/10.1016/j.actamat.2023.119634.

## References

[1] H. Gleiter, Nanocrystalline materials, Prog. Mater. Sci. 33 (4) (1989) 223–315, http://dx.doi.org/10.1016/0079-6425(89)90001-7, URL https://www.sciencedirect.com/science/article/pii/0079642589900017.
[2] M. Meyers, A. Mishra, D. Benson, Mechanical properties of nanocrystalline materials, Prog. Mater. Sci. 51 (4) (2006) 427–556.
[3] R. Würschum, K. Reimann, P. Farber, Correlation between interfacial structure, tracer diffusion and crystal growth in nanocrystalline metals and alloys, in: Defect and Diffusion Forum, Vol. 143, Trans Tech Publ, 1997, pp. 1463–1468.
[4] H. Gleiter, Nanoglasses: a new kind of noncrystalline materials, Beilstein J. Nanotechnol. 4 (2013) 517–533, http://dx.doi.org/10.3762/bjnano.4.61.
[5] H. Gleiter, T. Schimmel, H. Hahn, Nanostructured solids–from nano-glasses to quantum transistors, Nano Today 9 (1) (2014) 17–68.
[6] R. Witte, T. Feng, J. Fang, A. Fischer, M. Ghafari, R. Kruk, R. Brand, D. Wang, H. Hahn, H. Gleiter, Evidence for enhanced ferromagnetism in an iron-based nanoglass, Appl. Phys. Lett. 103 (7) (2013) 073106.
[7] J. Jing, A. Kramer, R. Birringer, H. Gleiter, U. Gonser, Modified atomic structure in a Pd70Fe3Si27 nanoglass: A Mössbauer study, J. Non-Cryst. Solids 113 (2) (1989) 167–170.
[8] H. Gleiter, Nanocrystalline solids, J. Appl. Crystallogr. 24 (2) (1991) 79–90.
[9] H. Gleiter, Are there ways to synthesize materials beyond the limits of today? Metall. Mater. Trans. A 40 (2009) 1499–1509.
[10] N. Chen, R. Frank, N. Asao, D. Louzguine-Luzgin, P. Sharma, J. Wang, G. Xie, Y. Ishikawa, N. Hatakeyama, Y. Lin, et al., Formation and properties of au-based nanograined metallic glasses, Acta Mater. 59 (16) (2011) 6433–6440.

[11] Z. Śniadecki, D. Wang, Y. Ivanisenko, V. Chakravadhanula, C. Kübel, H. Hahn, H. Gleiter, Nanoscale morphology of Ni50Ti45Cu5 nanoglass, Mater. Charact. 113 (2016) 26–33.

[12] W. Yao, Q. Cao, S. Liu, X. Wang, H. Fecht, A. Caron, D. Zhang, J. Jiang, Tailoring nanostructured Ni-Nb metallic glassy thin films by substrate temperature, Acta Mater. 194 (2020) 13–26.

[13] S. Dina, U. Geyer, G. v. Minnigerode, Macroscopic intrinsic stress formation in amorphous CuTi films, Ann. Phys. 507 (7) (1995) 623–633.

[14] U. Geyer, U. Von Hülsen, P. Thiyagarajan, Surface roughening and columnar growth of thin amorphous CuTi films, Appl. Phys. Lett. 70 (13) (1997) 1691–1693.

[15] O. Adjaoud, K. Albe, Microstructure formation of metallic nanoglasses: Insights from molecular dynamics simulations, Acta Mater. 145 (2018) 322–330.

[16] Z.D. Sha, L.C. He, Q.X. Pei, H. Pan, Z.S. Liu, Y.W. Zhang, T.J. Wang, On the notch sensitivity of CuZr nanoglass, J. Appl. Phys. 115 (16) (2014).

[17] S.H. Nandam, Y. Ivanisenko, R. Schwaiger, Z. Śniadecki, X. Mu, D. Wang, R. Chellali, T. Boll, A. Kilmametov, T. Bergfeldt, et al., Cu-Zr nanoglasses: Atomic structure, thermal stability and indentation properties, Acta Mater. 136 (2017) 181–189.

[18] H. Voigt, A. Rigoni, E. Boltynjuk, M.R. Chellali, B. Tyler, H. Rösner, S. Divinski, H. Hahn, G. Wilde, Evidence for glass–glass interfaces in a columnar Cu–Zr nanoglass, Adv. Funct. Mater. (2023) 2302386.

[19] J. Bokeloh, S.V. Divinski, G. Reglitz, G. Wilde, Tracer measurements of atomic diffusion inside shear bands of a bulk metallic glass, Phys. Rev. Lett. 107 (23) (2011) 235503.

[20] I. Binkowski, G.P. Shrivastav, J. Horbach, S.V. Divinski, G. Wilde, Shear band relaxation in a deformed bulk metallic glass, Acta Mater. 109 (2016) 330–340.

[21] A. Hassanpour, M. Vaidya, S.V. Divinski, G. Wilde, Impact of cryogenic cycling on tracer diffusion in plastically deformed Pd40 Ni40 P20 bulk metallic glass, Acta Mater. 209 (2021) 116785.

[22] D. Gaertner, L. Belkacemi, V.A. Esin, F. Jomard, A.A. Fedotov, J. Schell, J.V. Osinskaya, A.V. Pokoev, C. Duhamel, A. Paul, S.V. Divinski, Techniques of tracer diffusion measurements in metals, alloys and compounds, Diff. Found. 29 (2021) 31–73, http://dx.doi.org/10.4028/www.scientific.net/DF.29.31.

[23] J. Horvath, K. Pfahler, W. Ulfert, W. Frank, H. Mehrer, 59Fe tracer self-diffusion in amorphous fe-Ni-b alloys, J. Phys. Colloques 46 (C8) (1985) C8–645.

[24] W. Dörner, H. Mehrer, Tracer diffusion and thermal stability in amorphous Co-Zr and their relevance for solid-state amorphization, Phys. Rev. B 44 (1) (1991) 101.

[25] F. Faupel, Diffusion in non-crystalline metallic and organic media, Phys. Status Solidi (a) 134 (1) (1992) 9–59.

[26] H. Mehrer, Diffusion in intermetallics, Mater. Trans. JIM 37 (6) (1996) 1259–1280.

[27] A.K. Tyagi, M.-P. Macht, V. Naundorf, Self diffusion measurements of nickel in Fe40Ni38Mo4B18 glass by secondary ion mass spectrometry, Scr. Metall. Mater. 24 (12) (1990) 2369–2374.

[28] K. Rätzke, P.W. Hüppe, F. Faupel, Transition from single-jump type to highly cooperative diffusion during structural relaxation of a metallic glass, Phys. Rev. Lett. 68 (15) (1992) 2347.

[29] T. Zumkley, V. Naundorf, M.-P. Macht, G. Frohberg, Effect of reversible structural relaxation on diffusion in a ZrTiCuNiBe bulk glass, Scr. Mater. 45 (4) (2001) 471–477.

[30] P. Fielitz, M.-P. Macht, V. Naundorf, G. Frohberg, Diffusion in ZrTiCuNiBe bulk glasses at temperatures around the glass transition, J. Non-Cryst. Solids 250 (1999) 674–678.

[31] S. Sharma, F. Faupel, Correlation between effective activation energy and pre-exponential factor for diffusion in bulk metallic glasses, J. Mater. Res. 14 (8) (1999) 3200–3203.

[32] H. Mehrer, Diffusion in Solids: Fundamentals, Methods, Materials, Diffusion-Controlled Processes, Vol. 155, Springer Science & Business Media, 2007.

[33] J. Crank, The Mathematics of Diffusion, Oxford University Press, 1979.

[34] Y. Amouyal, S.V. Divinski, Y. Estrin, E. Rabkin, Short-circuit diffusion in an ultrafine-grained copper–zirconium alloy produced by equal channel angular pressing, Acta Mater. 55 (17) (2007) 5968–5979.

[35] J.C. Fisher, Calculation of diffusion penetration curves for surface and grain boundary diffusion, J. Appl. Phys. 22 (1) (1951) 74–77.

[36] L. Harrison, Influence of dislocations on diffusion kinetics in solids with particular reference to the alkali halides, Trans. Faraday Soc. 57 (1961) 1191–1199.

[37] A. Paul, T. Laurila, V. Vuorinen, S.V. Divinski, Thermodynamics, diffusion and the kirkendall effect in solids, in: Thermodyn. Diffus. Kirkendall Eff. Solids, vol. 9783319074610, Springer International Publishing, 2014, pp. 1–530, http://dx.doi.org/10.1007/978-3-319-07461-0.

[38] N.A. Stolwijk, C. Poisson, J. Bernardini, Segregation-controlled kinetics of fast impurity diffusion in polycrystalline solids, J. Phys.: Condens. Matter 8 (1996) 5843, http://dx.doi.org/10.1088/0953-8984/8/32/005.

[39] C. Poisson, A. Rolland, J. Bernardini, N.A. Stolwijk, Diffusion of gold into polycrystalline silicon investigated by means of the radiotracer 195Au, J. Appl. Phys. 80 (11) (1996) 6179–6187, http://dx.doi.org/10.1063/1.363712, arXiv:https://pubs.aip.org/aip/jap/article-pdf/80/11/6179/8052244/6179_1_online.pdf.

[40] K. Knorr, M.P. Macht, K. Freitag, H. Mehrer, Self-diffusion in the amorphous and supercooled liquid state of the bulk metallic glass Zr46.75Ti8.25Cu7.5Ni10Be27.5, J. Non-cryst. Solids 250 (1999) 669–673, URL https://api.semanticscholar.org/CorpusID:135775911.

[41] F. Faupel, W. Frank, M.-P. Macht, H. Mehrer, V. Naundorf, K. Rätzke, S.K. Schober, H. Teichler, Diffusion in metallic glasses and supercooled melts, Rev. Modern Phys. 75 (1) (2003) 237.

[42] J. Horvath, J. Ott, K. Pfahler, W. Ulfert, Tracer diffusion in amorphous alloys, Mater. Sci. Eng. 97 (1988) 409–413.

[43] H. Hahn, R. Averback, H.-M. Shyu, Diffusion studies in amorphous NiZr alloys and their relevance for solid state amorphizing reactions, J. Less Common Metals 140 (1988) 345–352.

[44] S. Frank, S. Divinski, U. Södervall, C. Herzig, Ni tracer diffusion in the B2-compound NiAl: influence of temperature and composition, Acta Mater. 49 (8) (2001) 1399–1411, http://dx.doi.org/10.1016/S1359-6454(01)00037-4, URL https://www.sciencedirect.com/science/article/pii/S1359645401000374.

[45] A. Van den Beukel, On the parameters governing atomic mobility in metallic glasses, Phys. Status Solidi A 128 (2) (1991) 285–293.

[46] C. Nagel, K. Rätzke, E. Schmidtke, J. Wolff, U. Geyer, F. Faupel, Free-volume changes in the bulk metallic glass Zr 46.7 Ti 8.3 Cu 7.5 Ni 10 Be 27.5 and the undercooled liquid, Phys. Rev. B 57 (17) (1998) 10224.

[47] A.R. Yavari, A. Le Moulec, A. Inoue, N. Nishiyama, N. Lupu, E. Matsubara, W.J. Botta, G. Vaughan, M. Di Michiel, Å. Kvick, Excess free volume in metallic glasses measured by X-ray diffraction, Acta Mater. 53 (6) (2005) 1611–1619.

[48] A. Slipenyuk, J. Eckert, Correlation between enthalpy change and free volume reduction during structural relaxation of Zr55Cu30Al10Ni5 metallic glass, Scr. Mater. 50 (1) (2004) 39–44.

[49] G. Wilde, G.P. Görler, R. Willnecker, H.J. Fecht, Calorimetric, thermomechanical, and rheological characterizations of bulk glass-forming Pd 40 Ni 40 P 20, J. Appl. Phys. 87 (3) (2000) 1141–1152.

[50] J. Bünz, G. Wilde, Direct measurement of the kinetics of volume and enthalpy relaxation of an Au-based bulk metallic glass, J. Appl. Phys. 114 (22) (2013).